

ARTICLE

Open Access

Synchronous detection of dual signals based on constant-drive technique of weakly coupled resonators

Han Li¹, Zhao Zhang¹, PeiYuan Zhu¹, GuoHua Zhang¹, Yongcun Hao¹✉ and Honglong Chang¹✉

Abstract

The demand for highly sensitive and accurate sensors has grown significantly, particularly in the field of Micro-Electro-Mechanical Systems technology. Mode-localized sensors based on weakly coupled resonators have garnered attention for their high sensitivity through amplitude ratio outputs. However, when measuring multiple signals by weakly coupled resonators, different signals can interfere with each other, causing high cross-sensitivity. This cross-sensitivity greatly complicates signal separation and makes accurate measurement extremely difficult, impacting system performance. To address this issue, the study proposes an innovative constant-drive technique of weakly coupled resonators. This technique significantly reduces crosstalk between signals while maintaining high sensitivity of amplitude ratio output. The method is theoretically validated by analyzing amplitude ratios under signal perturbations in non-damped conditions, demonstrating perfect elimination of cross-interference. Finite element analysis under damping conditions further validated the constant-drive technique, showing a cross-sensitivity of 0.054%, nearly three orders of magnitude lower than that of mode-localized sensors. Experimental validation confirmed the effectiveness of the proposed technique, with the cross-sensitivity of the mode-localized method measured at 26.3% and 28.7%, respectively, while the constant-frequency drive achieved significantly lower values of 3.1% and 1.1%. This demonstrates a successful reduction in cross-sensitivity by an order of magnitude, meeting the performance requirements for typical MEMS biaxial sensor applications. This method is highly significant for mode-localized sensors, offering potential for developing multi-signal measurement devices like multi-axis accelerometers, force sensor, electric field sensor and mass sensor.

Introduction

In recent years, the demand for highly sensitive and accurate sensors has surged, particularly in the fields of Micro-Electro-Mechanical Systems (MEMS) technology. These advancements are driven by the growing need for precise measurements in various applications, such as Automotive Safety and Navigation^{1,2}, environmental monitoring^{3,4}, biomedical diagnostics⁵, and industrial automation^{6,7}. MEMS sensors offer advantages like miniaturization, low power consumption, and the ability to

integrate multiple functions on a single chip, making them highly attractive for modern sensing applications. As the complexity of these applications increases, so does the requirement for sensors capable of detecting multiple signals simultaneously.

Mode-localized sensors have emerged as a popular solution for signal detection due to their high sensitivity⁸. Mode localization^{9–12} is an extension of Anderson localization¹³ in structure dynamics and is usually manifested in the periodic structure of weakly coupled resonators (WCRs). When a small disorder is applied, the mode shape of the WCRs will be drastically changed and the vibration energy will mostly be confined to some specific modes of the WCRs. Various MEMS sensors based on the mode localization phenomenon have been widely used in various applications such as accelerometers^{14–19}, mass

Correspondence: Yongcun Hao (haoyongcun@nwpu.edu.cn) or Honglong Chang (changhl@nwpu.edu.cn)

¹Ministry of Education Key Laboratory of Micro and Nano Systems for Aerospace, School of Mechanical Engineering, Northwestern Polytechnical University, Xi'an 710072, China

© The Author(s) 2025



Open Access This article is licensed under a Creative Commons Attribution-NonCommercial-NoDerivatives 4.0 International License, which permits any non-commercial use, sharing, distribution and reproduction in any medium or format, as long as you give appropriate credit to the original author(s) and the source, and provide a link to the Creative Commons license. You do not have permission under this license to share adapted material derived from this article or parts of it. The images or other third party material in this article are included in the article's Creative Commons license, unless indicated otherwise in a credit line to the material. If material is not included in the article's Creative Commons license and your intended use is not permitted by statutory regulation or exceeds the permitted use, you will need to obtain permission directly from the copyright holder. To view a copy of this license, visit <http://creativecommons.org/licenses/by-nc-nd/4.0/>.

sensors^{8,20}, electrometers^{21–24}, electric field strength sensors²⁵, electric current sensors²⁶ and voltage sensor²⁷.

However, conventional MEMS sensors, particularly those based on coupled resonators, face significant limitations when it comes to simultaneously measuring multiple signals. When multiple signals are input, they cause shifts in the sensor’s resonant frequencies, leading to significant cross-sensitivity due to mutual interference between the signals. This interference not only reduces measurement sensitivity and accuracy but also hampers the overall performance in practical applications. Therefore, achieving synchronous detection of different signals while maintaining the sensitivity of mode-localized sensors remains a key challenge in this field.

To tackle this challenge, this paper introduces a novel approach using weakly coupled resonators with a constant-drive technique. By stabilizing the resonator’s driving frequency, the method effectively reduces the cross-sensitivity, enabling precise synchronous detection of two distinct signals. This paper details the design, experimental validation, and performance analysis of the method, demonstrating its potential to improve mode-localized sensor functionality in multi-signal scenarios.

Results and discussion

Structure of the dual signals sensor

The schematic diagram of the dual signals sensor (DSS) structure is shown in Fig. 1a. The structure consists of WCRs, sense electrodes, drive electrodes, tune electrodes, and anchors. The core component is the WCRs, which comprises three individual resonators with equal stiffness

($k_1 = k_2 = k_3 = k$), connected by two couplers. The coupling stiffness between the resonators is significantly lower than the stiffness of the resonators themselves ($k_c \ll k$), allowing for weak coupling.

The three resonators are arranged horizontally and connected in series via the two couplers, with all resonators oscillating exclusively in the vertical direction. They are fixed at the anchors and activated by the drive electrodes. An AC signal is applied to the resonators through the drive electrodes, producing the output signal, which is detected by the sense electrodes.

The tune electrode adjusts the resonator’s stiffness by applying voltage, compensating for manufacturing variations to ensure same stiffness across all three resonators. In this paper, the two signals are input by applying voltage to the tune electrodes of resonator 1 and resonator 3. Both perturbations cause significant changes in the amplitude ratio between resonators 1, 2, and 3. Finally, the input voltage is determined by measuring the amplitude ratios $AR_1 (A_2/A_1)$ and $AR_2 (A_2/A_3)$, respectively. Table 1 presents the design parameters of the DSS.

Transduction mechanism

Figure 1b illustrates the equivalent mass-spring model of the DSS under ideal conditions (without damping). The stiffness and mass of the three resonators are identical ($k_1 = k_2 = k_3 = k$, $m_1 = m_2 = m_3 = m$). Two signals introduce stiffness disturbances to resonator 1 and resonator 3, respectively. The dynamic equation for the DSS is given in Eq. (1).

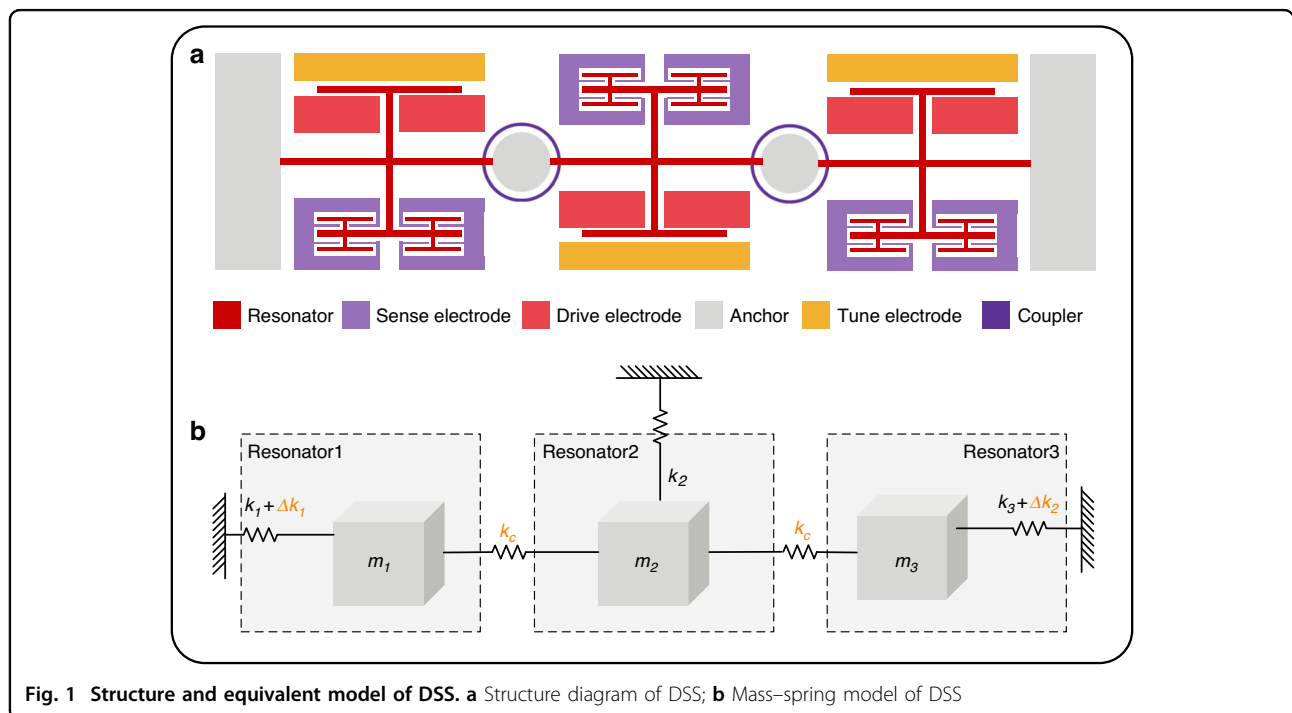


Table 1 Parameters of the DSS

Parameters	Value
Nominal frequency	22.9 kHz
Beams of resonators length	1200 μm
Beams of resonators width	12 μm
Coupler inner radius	305 μm
Coupler external radius	313 μm
Gap between drive comb	2.5 μm
Drive comb overlap length	11 μm
Gap between sense capacitor	2.5 μm
Sense capacitor length	110 μm
Gap between volt tune capacitor	2.5 μm

Figure 1b shows the equivalent mass and spring model of the DSS in ideal conditions (damping not considered). The stiffness and mass of three resonators are identical. Two signals cause stiffness perturbations to resonator 1 and resonator 3 (Δk_1 , Δk_2), respectively. The dynamic equation for the DSS is as Eq. (1).

$$\begin{bmatrix} m & 0 & 0 \\ 0 & m & 0 \\ 0 & 0 & m \end{bmatrix} \begin{bmatrix} \ddot{x}_1 \\ \ddot{x}_2 \\ \ddot{x}_3 \end{bmatrix} + \begin{bmatrix} k + k_c + \Delta k_1 & -k_c & 0 \\ -k_c & k + 2k_c & -k_c \\ 0 & -k_c & k + k_c + \Delta k_2 \end{bmatrix} \begin{bmatrix} x_1 \\ x_2 \\ x_3 \end{bmatrix} = \begin{bmatrix} 0 \\ 0 \\ 0 \end{bmatrix} \quad (1)$$

$$\begin{bmatrix} -m\omega^2 + k + k_c + \Delta k_1 & -k_c & 0 \\ -k_c & -m\omega^2 + k + 2k_c & -k_c \\ 0 & -k_c & -m\omega^2 + k + k_c + \Delta k_2 \end{bmatrix} \begin{bmatrix} A_1 \\ A_2 \\ A_3 \end{bmatrix} = 0 \quad (2)$$

The resonator undergoes simple harmonic motion, and by substituting the mode equation $x = A \sin(\omega t + \varphi)$ into Eq. (1), a linear system of equations for the amplitude, as shown in Eq. (2), can be derived.

The two disturbances, Δk_1 and Δk_2 , correspond to the amplitude ratio outputs as follows:

$$\begin{cases} AR_1 = \frac{A_2}{A_1} = \frac{-m\omega^2 + k + k_c + \Delta k_1}{k_c} \\ AR_2 = \frac{A_2}{A_3} = \frac{-m\omega^2 + k + k_c + \Delta k_2}{k_c} \end{cases} \quad (3)$$

The amplitude ratio AR_1 between resonator 2 and resonator 1, and the amplitude ratio AR_2 between resonator 2 and resonator 3, correspond to the two input disturbances Δk_1 and Δk_2 , respectively. From Eq. (3), it is

known that AR_1 is related to and the resonant frequency. The input of k_2 causes changes in omega, which in turn leads to changes in the output AR_1 . Similarly, k_1 affects AR_2 in the same way. This is the fundamental reason for the mutual interference between the two signals. The resonant frequency can be determined by setting the determinant of the coefficient matrix in Eq. (2) to zero. The result is as Eq. (4).

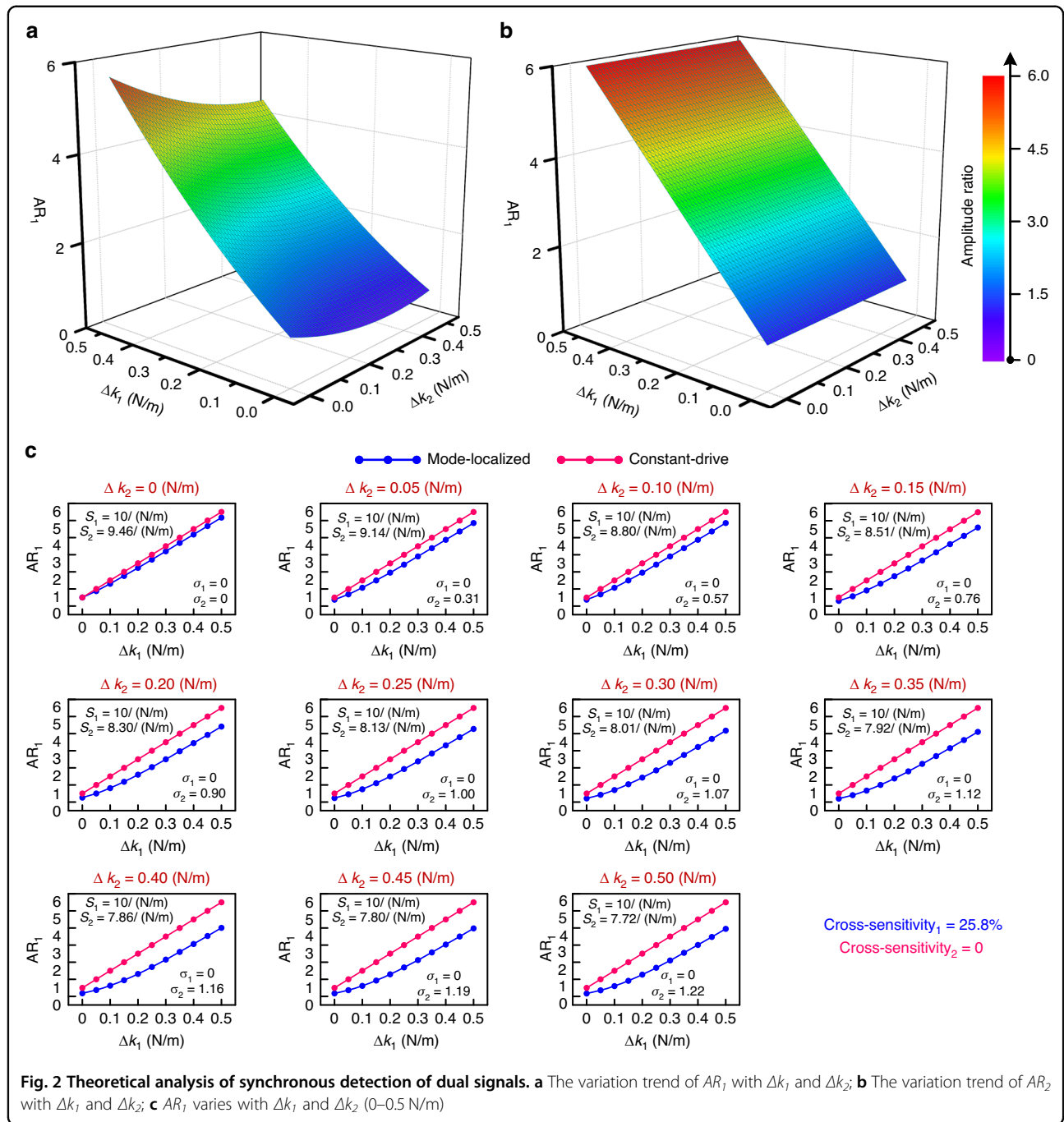
$$\begin{aligned} & (-m\omega^2 + k + k_c)^3 + (\Delta k_1 + \Delta k_2 + k_c)(-m\omega^2 + k + k_c)^2 \\ & + (\Delta k_1 \Delta k_2 + \Delta k_1 k_c + \Delta k_2 k_c - 2k_c^2)(-m\omega^2 + k + k_c) \\ & + \Delta k_1 \Delta k_2 k_c - k_c^2(\Delta k_1 + \Delta k_2) = 0 \end{aligned} \quad (4)$$

The amplitude ratio AR_1 between resonator 2 and resonator 1, and the amplitude ratio AR_2 between resonator 2 and resonator 3, correspond to the two input disturbances Δk_1 and Δk_2 , respectively. As shown in Eq. (3), AR_1 is related to the resonant frequency. The input of Δk_2 causes a change in ω , which in turn alters the output AR_1 . Similarly, Δk_1 affects AR_2 in the same way. This mutual interference between the two signals is the fundamental reason for their interaction. The resonant frequency can be determined by setting the determinant

of the coefficient matrix in Eq. (2) to zero, resulting in the following expression (4).

From Eq. (4), the first resonant frequency of the WCRs can be determined. Since the DSS structure is theoretically fully symmetrical, this paper focuses solely on analyzing the effects of Δk_1 and Δk_2 on the output of AR_1 . By Eq. (3) and Eq. (4), the relationship between k_1 and k_2 with respect to AR_1 can be derived. As shown in Fig. 2a, AR_1 has a linear relationship with Δk_1 , but decreases as Δk_2 increases. The larger the AR_1 , the greater the influence of k_2 on AR_1 . Therefore, it is not feasible to simultaneously detect two signals by mode-localized phenomenon.

From Eq. (3), it can be concluded that the mutual interference between the two signals is due to changes in the resonant frequency caused by the signals. To address this, this paper proposes a constant-drive mode for



weakly coupled resonators, where the resonators are driven at their natural resonant frequencies without altering the driving frequency. By substituting $\Delta k_1 = 0$ and $\Delta k_2 = 0$ into Eq. (4), the natural resonant frequencies of the undisturbed resonators can be obtained, as shown in Eq. (6).

$$\begin{cases} \omega_1 = \sqrt{\frac{k}{m}} \\ \omega_2 = \sqrt{\frac{k+k_c}{m}} \\ \omega_3 = \sqrt{\frac{k+3k_c}{m}} \end{cases} \quad (6)$$

$$(-m\omega^2 + k + k_c)(-m\omega^2 + k)(-m\omega^2 + 3k_c) = 0$$

(5)

By substituting Eq. (6) into Eq. (3), the relationship between AR_I and Δk_I at three different frequencies is

derived, as shown in Eq. (7). In constant-drive mode, the sensitivity of Δk_1 to AR_1 is $1/k_c$, which is the same as in the mode localization effect, demonstrating that this method does not suffer from a loss of sensitivity. The relationship between Δk_1 and Δk_2 for AR_1 in constant-drive mode is shown in Fig. 2b. Therefore, the sensitivity of AR_1 to Δk_2 is zero, indicating that there is no interference between the detection of Δk_1 and Δk_2 .

$$\begin{cases} AR_{11} = \frac{A_2}{A_1} = \frac{k_c + \Delta k_1}{k_c} \\ AR_{12} = \frac{A_2}{A_1} = \frac{\Delta k_1}{k_c} \\ AR_{13} = \frac{A_2}{A_1} = \frac{-2k_c + \Delta k_1}{k_c} \end{cases} \quad (7)$$

To more clearly illustrate the differences between the two methods, this paper quantitatively analyzes the detection interference of the two signals over a range of 0–0.5 N/m, with a step of 0.05 N/m. In this analysis, the spring constant k is 290 N/m, the mass m is 1.4×10^{-8} kg, and the coupling strength k_c is 0.1 N/m.

As shown in Fig. 2c, the sensitivity of the constant-drive mode is 10 N/m and remains constant with Δk_2 increases, with no deviation in AR_1 caused by Δk_2 . Therefore, there is not cross-sensitivity for constant-drive mode. In contrast, the sensitivity of the mode-localized method is 9.46 N/m when $k_2 = 0$, but sensitivity decreases with k_2 increases. The maximum deviation in AR_2 caused by Δk_1 is 1.22, resulting in a sensitivity of AR_2 to Δk_1 being 2.44 N/m, which corresponds to a cross-sensitivity of 25.8%.

The constant-drive mode sensitivity is higher than that of the mode-localized method, which is due to a nonlinear region at the mode-localized method's lower initial working point²⁸, lowering the overall sensitivity. Thus, the constant-drive mode proposed in this paper not only preserves the sensitivity of the Mode-localized sensor but also eliminates interference between the two signals.

Finite element analysis of the DSS

Through the theoretical analysis the effectiveness of the constant-drive mode for dual-signal synchronous detection can be established. However, this theoretical analysis is based on undamped conditions, leaving the impact of damping interference on the dual signals unclear. Due to the complexity of theoretical analysis in the presence of damping, this paper employs finite element simulation (FEM) to analyze both methods. This approach not only verifies the level of interference in detecting the two signals within a damped system but also reveals the amplitude variation patterns of each resonator, contributing to a better understanding of the overall sensing process.

The results of the FEM simulation are shown in Fig. 3. Figure 3a displays the three natural frequencies of the

DSS, with the resonant frequencies of the three resonators being 22,937.07 Hz, 22,940.86 Hz, and 22,946.31 Hz, respectively. The corresponding initial amplitude ratios are 1, 0, and 2, which align with Eq. (7).

In the constant-drive mode, the amplitude variation of resonators 1, 2, and 3 with respect to changes in Δk_1 and Δk_2 is shown in Fig. 3b, c, and d, respectively. The amplitudes of the three resonators decrease as Δk_1 and Δk_2 increase. Specifically, the amplitude of resonator 1 decreases more rapidly with Δk_1 than with Δk_2 , while conversely, the amplitude of resonator 3 decreases more rapidly with Δk_2 than Δk_1 . Thus, unlike the mode-localized effect, where energy is redistributed throughout the system, the constant-drive method essentially represents the dissipation of overall energy. Both disturbances reduce the amplitudes of all three resonators. However, for the primary disturbance, such as Δk_1 affecting resonator 1, the faster decrease in amplitude provides AR_1 with high sensitivity to Δk_1 . On the other hand, Δk_2 causes the amplitudes of resonators 1 and 2 to decrease proportionally, keeping AR_1 unchanged and thus eliminating the interference from k_2 on AR_1 . The trends of AR_1 and AR_2 with respect to Δk_1 and Δk_2 are shown in the Fig. 3e, f. The Fig. 3e, f indicates that AR_1 and AR_2 exhibit a good linear relationship with Δk_1 and Δk_2 , respectively, and are essentially unaffected by changes in the other signal, consistent with Fig. 2b.

The effect of Δk_1 on AR_2 in the mode-localized method is shown in the Fig. 3g. Both theoretical and FEM simulation results indicate the same trend: as Δk_1 increases, the change in AR_2 also increases, but the rate of change slows down, with results of 1.22 and 1.04, respectively. The discrepancy between these results may be due to differences in coupling stiffness. In the constant-drive mode, the effect of Δk_1 on AR_2 is shown in the Fig. 3h. Theoretically, Δk_1 has no impact on AR_2 . However, in simulations, Δk_1 influences AR_2 in the same pattern as the mode-localized method but with significantly lower intensity, resulting in a slight effect with a cross-sensitivity of 0.054%. The energy redistribution in the mode-localized effect involves not only the transfer of energy between two resonators but also the coupling between different modes within each resonator. In the absence of damping, these modes remain completely decoupled, and the constant-drive mode effectively isolates energy transfer between different resonators, resulting in zero cross-sensitivity. However, when damping is introduced, it alters the mode energy distribution, leading to energy leakage from one mode to another. This disrupts the perfect isolation achieved in the undamped case, resulting cross-sensitivity to emerge. As a result, despite being significantly lower in magnitude compared to the mode-localized method, a similar pattern of cross-sensitivity is observed in simulations,

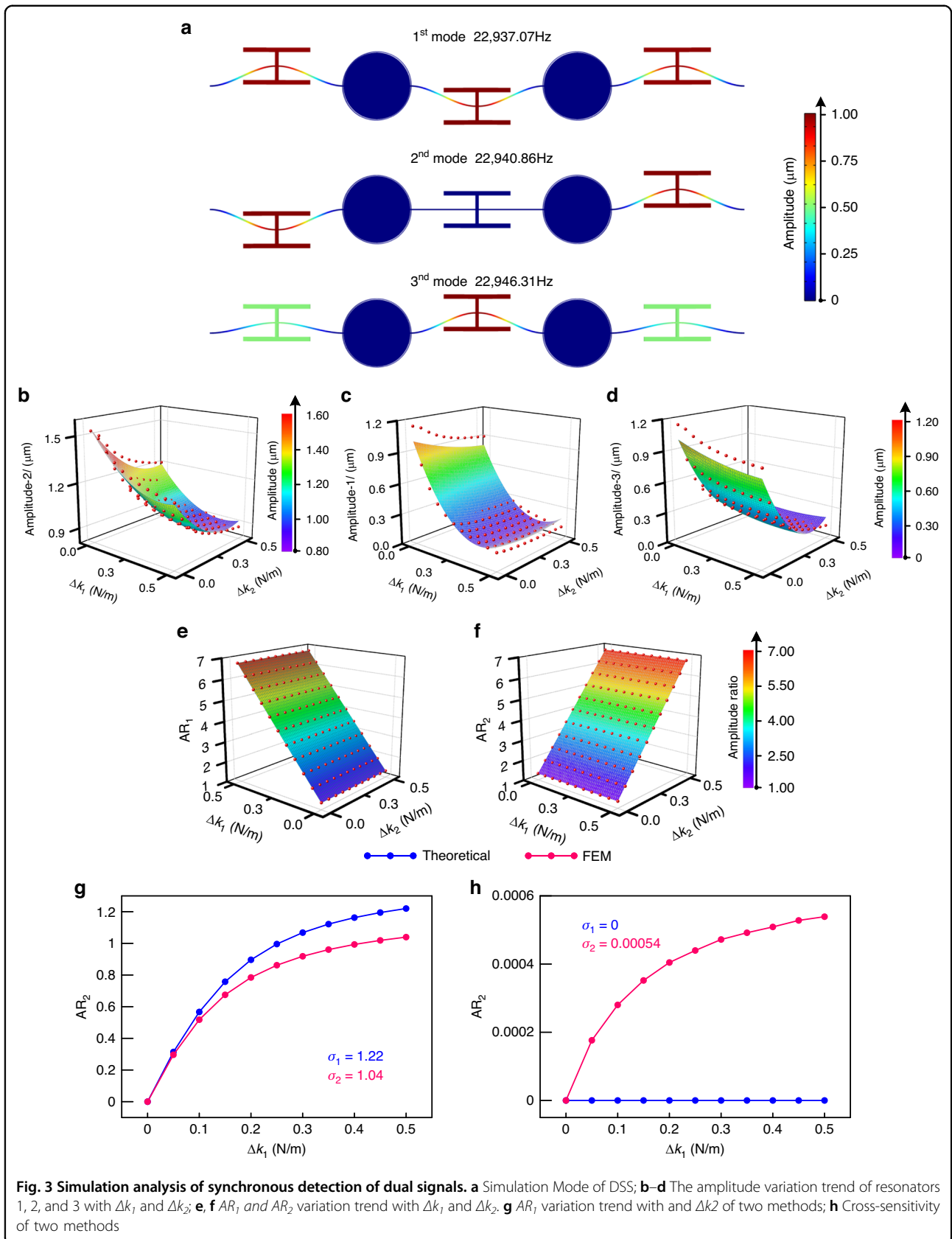


Fig. 3 Simulation analysis of synchronous detection of dual signals. **a** Simulation Mode of DSS; **b–d** The amplitude variation trend of resonators 1, 2, and 3 with Δk_1 and Δk_2 ; **e, f** AR_1 and AR_2 variation trend with Δk_1 and Δk_2 . **g** AR_1 variation trend with and Δk_2 of two methods; **h** Cross-sensitivity of two methods

driven in damping-induced condition. A similar energy transfer mechanism has been reported in related studies²⁹.

This paper clarifies the amplitude variation patterns of the three resonators through FEM simulation, explains the detection mechanism of the constant-drive mode for dual-signal detection, and reaffirms the effectiveness of the constant-drive mode in reducing crosstalk between the two signals, decreasing the cross-sensitivity by over 1000 times.

Experimental principle and environment

An experimental schematic of a DSS is displayed in Fig. 4. As shown in Fig. 4a, the experiment is performed in a vacuum chamber with a pressure of 0.022 Pa. DSS incorporates three resonators, each designed with differential outputs to minimize common mode noise³⁰. As depicted in Fig. 4b, the differential signals are amplified using charge amplifiers (AD8605) and instrumentation amplifiers (AD8221). The device and interface circuit are powered by an external power supply. An AC drive signal is provided through a lock-in amplifier, which also receives the signal from the interface circuit. Since the lock-in amplifier has only two input channels, it can only receive signals from two resonators at a time. Therefore,

the selected approach is to keep resonator 2 constantly connected, while resonators 1 and 3 are alternately connected.

In this experiment, the lock-in amplifier was used to provide an AC drive signal and to perform detection using both the mode-localized method and the constant-drive mode. In the mode-localized method, the lock-in amplifier’s PID module is used for closed-loop control of the DSS, continuously tracking the DSS resonant frequency as the two signals are input. In the constant-drive mode, the lock-in amplifier’s open-loop frequency sweep function is initially used to determine the resonators’ operating frequency, which is then set as the AC drive frequency and kept constant.

As shown in Fig. 4c. The phase-locked amplifier begins by generating a reference signal from a high-precision crystal oscillator. This reference signal is then compared with the signal produced by a voltage-controlled oscillator (VCO). The phase difference between the two signals is detected and processed by a phase-locked loop (PLL), which adjusts the VCO’s frequency to match the reference signal. The PLL continuously fine-tunes the VCO, ensuring the output signal’s frequency remains stable and locked to the reference, providing high accuracy and stability.

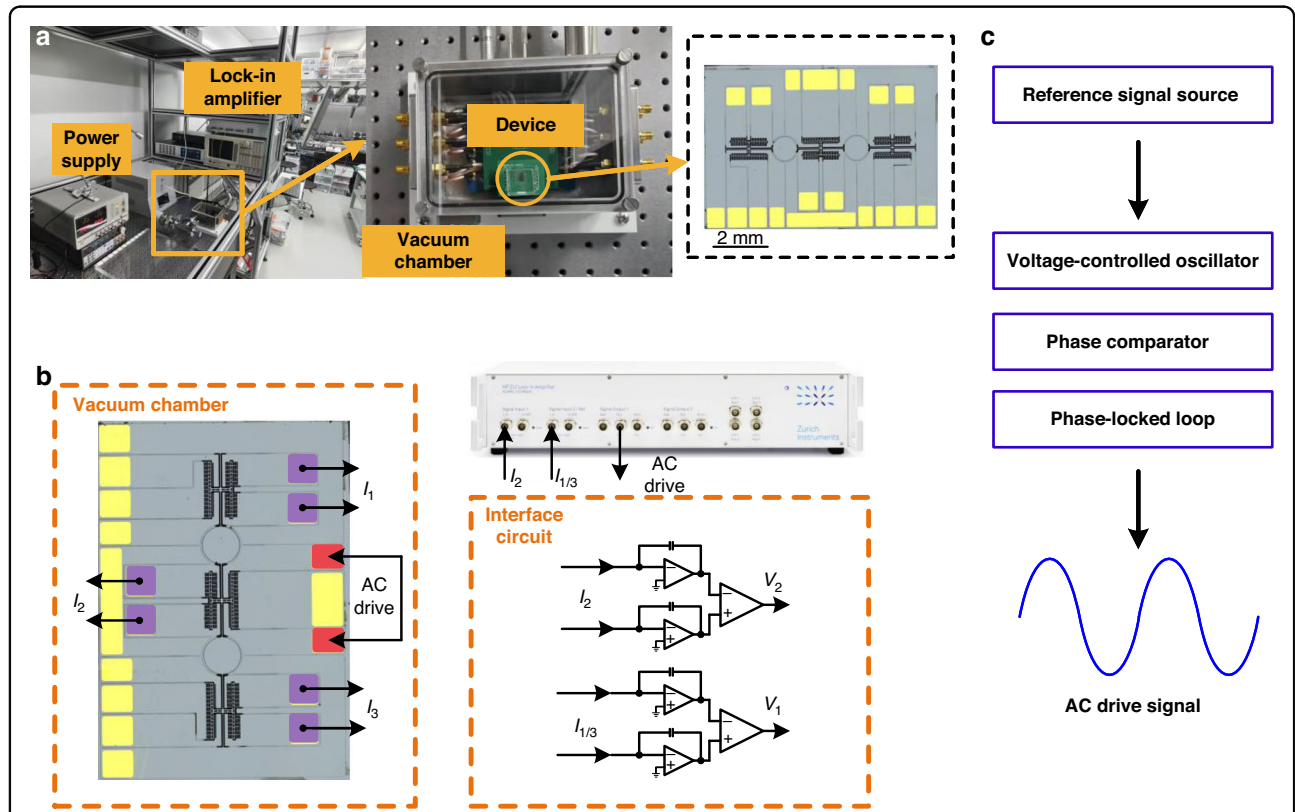


Fig. 4 Experimental setup and procedure. **a** Photo of the experimental environment DSS; **b** Experimental principle of the DSS; **c** The process of stabilizing the driving force

Amplitude frequency response

A 10 V DC bias voltage was applied to the weakly coupled resonators, and then the stiffness of the three resonators was equalized by adjusting the stiffness of resonators 1 and 3 by two tune electrodes positioned around them. After the adjustment, the tuning voltages

for resonators 1 and 3 were 21.611 V and 9.36 V, respectively.

The study tested the frequency response of the resonators under different tuning voltages to better analyze the two methods. As shown in the Fig. 5a–d, in the mode-localized method, the amplitude of Resonator 1 increases

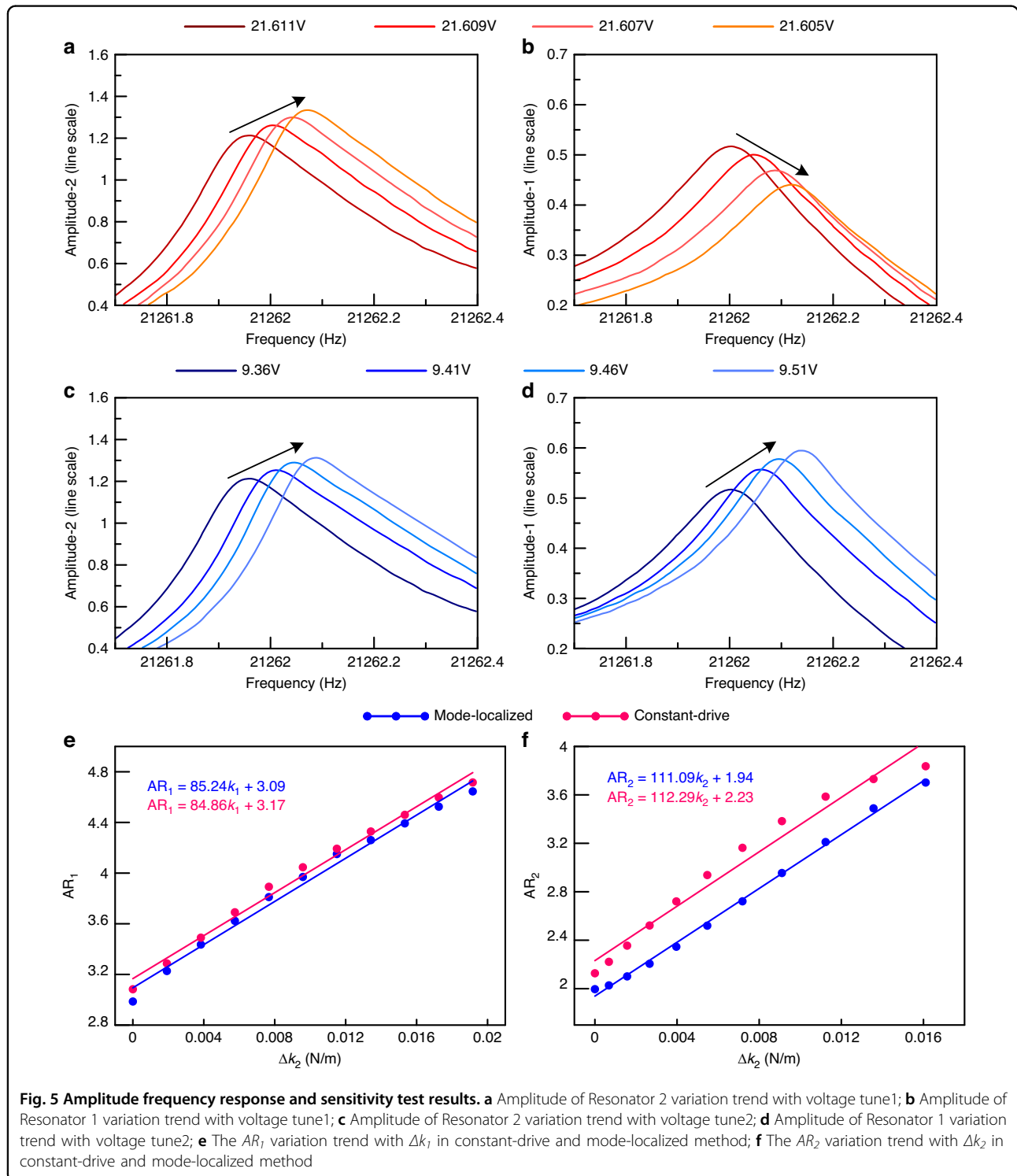


Fig. 5 Amplitude frequency response and sensitivity test results. **a** Amplitude of Resonator 2 variation trend with voltage tune1; **b** Amplitude of Resonator 1 variation trend with voltage tune1; **c** Amplitude of Resonator 2 variation trend with voltage tune2; **d** Amplitude of Resonator 1 variation trend with voltage tune2; **e** The AR_1 variation trend with Δk_1 in constant-drive and mode-localized method; **f** The AR_2 variation trend with Δk_2 in constant-drive and mode-localized method

with the input of Δk_1 , while the amplitude of Resonator 2 decreases. With the input of Δk_2 the amplitudes of both Resonators 1 and 2 increase. In contrast, for the constant-drive method, regardless of whether Δk_1 or Δk_2 is input, the amplitudes at the initial resonance frequencies of both resonators will reduce. Therefore, the fundamental difference between the two methods lies in the fact that modal localization detects the signal through energy redistribution, while constant-drive detects it through energy loss. The response of Resonator 3 is almost identical to that of Resonator 1, so it is not presented here. In the following sections, the sensitivity and cross-sensitivity of the two methods will be tested and analyzed.

Sensitivity experiment

The voltage sensitivity of the resonator is directly proportional to the difference between the tune voltage and the DC bias voltage. Due to variations in these voltage differences, there can be a significant disparity in voltage sensitivity between resonator 1 and resonator 3. Therefore, voltage sensitivity directly to calculate cross-sensitivity is not appropriate. This study converts voltage into stiffness for sensitivity analysis. The conversion relationship between voltage and stiffness is shown in Eq. (8). To ensure that the input stiffness ranges for the two signals correspond, the input ranges for resonators 1 and 3 are set as follows: 21.611 V to 21.591 V with a step size of 2 mV, and 9.36 V to 9.86 V with a step size of 5 mV. The relationship between voltage and stiffness signals is shown in Table 2.

$$|k_e| = \frac{\varepsilon A}{d^3} = (V_{dc} - V_{tune})^2 \frac{\varepsilon A}{d^3} \quad (8)$$

Sensitivity tests were conducted on the DSS in both constant-drive mode and mode-localized method, with the results shown in Fig. 5. Figure 5e displays the output relationship between AR_1 and Δk_1 in both modes, with no Δk_2 input during the testing process. As Δk_1 increases from 0 to 0.0192 N/m, in constant-drive mode, AR_1 increases from 2.99 to 4.64, while in mode-localized method, AR_1 increases from 3.08 to 4.72. The fitted lines for the constant-drive and mode-localized methods are represented by Eqs. (9) and (10), with sensitivities of 85.24/(N/m) and 84.86/(N/m), respectively.

Figure 5f displays the output relationship between AR_2 and Δk_2 in both modes, with no Δk_1 input during the testing process. As Δk_2 increases from 0 to 0.0161 N/m, in constant-drive mode, AR_2 increases from 2.00 to 3.70, while in mode-localized method, AR_2 increases from 2.13 to 3.84.

The fitted lines for the constant-drive mode and mode-localized methods are represented by Eqs. (11) and (12),

Table 2 Conversion relationship between voltage and stiffness

Voltage tune1 (V)	Stiffness 1 (N/m)	Voltage tune2 (V)	Stiffness 2 (N/m)
21.611	0.0000	9.86	0.0000
21.609	0.0019	9.81	0.0007
21.607	0.0038	9.76	0.0016
21.605	0.0058	9.71	0.0027
21.603	0.0077	9.65	0.0040
21.601	0.0096	9.61	0.0055
21.599	0.0115	9.56	0.0072
21.597	0.0134	9.51	0.0091
21.595	0.0153	9.46	0.0112
21.593	0.0172	9.41	0.0136
21.591	0.0192	9.36	0.0161

with sensitivities of 111.09/(N/m) and 112.29/(N/m), respectively. The experimental results are consistent with the FEM simulation results, indicating that the sensitivity of constant-drive method is basically consistent with the mode-localized method.

$$AR_1 = 85.24k_1 + 3.09 \quad (9)$$

$$AR_1 = 84.86k_1 + 3.17 \quad (10)$$

$$AR_2 = 111.09k_2 + 1.94 \quad (11)$$

$$AR_2 = 112.29k_2 + 2.23 \quad (12)$$

Dual signal synchronization detection Experiment

The input ranges for resonators 1 and 3 are set as follows: 21.611 V to 21.591 V with a step size of 4 mV, and 9.36 V to 9.86 V with a step size of 10 mV. The interference test results for the two signals in the constant-drive mode are shown in Fig. 6. When resonators 1 and 2 are connected to the lock-in amplifier, the amplitude variation of resonators 2 and 1 with respect to k_1 and k_2 is shown in Fig. 6a, b. As Δk_1 increases from 0 to 0.0192 N/m and Δk_2 increases from 0 to 0.0161 N/m, the amplitude of resonator 2 decreases from 186.5 mV to 142.4 mV, and the amplitude of resonator 1 decreases from 59.7 mV to 30.3 mV. The corresponding AR_1 is shown in Fig. 6e. When $\Delta k_2 = 0$, as k_1 increases from 0 to 0.0192 N/m, AR_1 increases from 3.126 to 4.656. However, with the input of Δk_2 , AR_1 also responds to Δk_2 . The variation trend of AR_1 with respect to Δk_2 is shown in Fig. 6g. As Δk_2 increases from 0 to 0.0161 N/m, the deviation produced by AR_1 gradually increases. The cross-sensitivity generated by

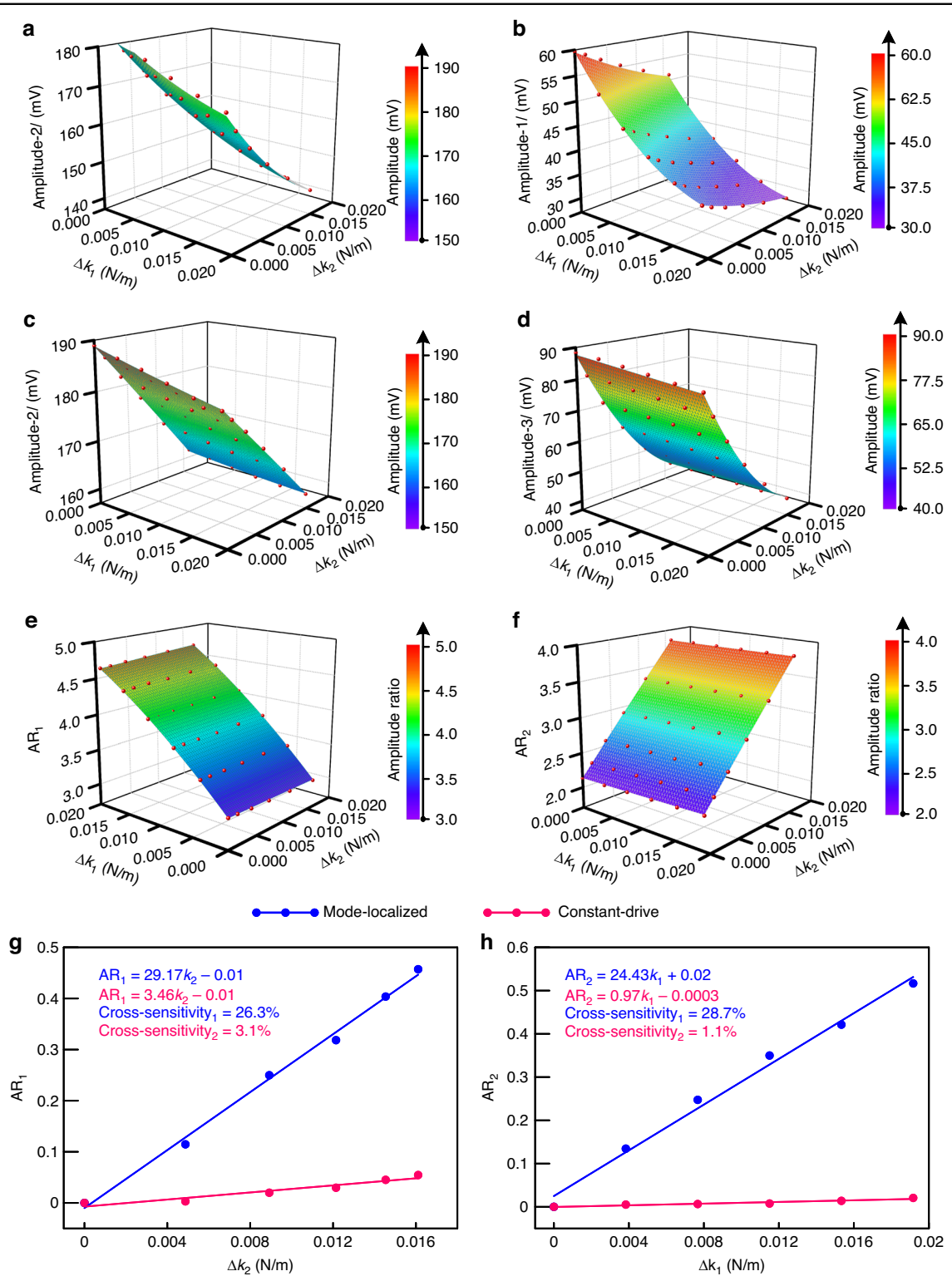


Fig. 6 Results of synchronous detection of dual signals. a–d The amplitude variation trend of resonators 1, 2, and 3 with Δk_1 and Δk_2 ; **e, f** AR_1 and AR_2 variation trend with Δk_1 and Δk_2 ; **g** AR_1 variation trend with and Δk_2 in constant-drive and mode-localized methods; **h** AR_2 variation trend with and Δk_1 in constant-drive and mode-localized methods

mode-localized and constant-drive methods are 26.3% and 3.1%, respectively.

When resonators 2 and 3 are connected to the lock-in amplifier, the amplitude variation of resonators 2 and 1 with respect to Δk_1 and Δk_2 is shown in Fig. 6c, d. As Δk_1 increases from 0 to 0.0192 N/m and Δk_2 increases from 0 to 0.0161 N/m, the amplitude of resonator 2 decreases from 189.0 mV to 161.7 mV, and the amplitude of resonator 1 decreases from 88.4 mV to 42.1 mV. The corresponding AR_2 is shown in Fig. 6f. When $k_1 = 0$, as Δk_2 increases from 0 to 0.0161 N/m, AR_2 increases from 2.137 to 3.844. However, with the input of Δk_2 , AR_2 also responds to Δk_1 . The variation trend of AR_2 with respect to Δk_1 is shown in Fig. 6h. As Δk_2 increases from 0 to 0.0192 N/m, the deviation produced by AR_2 gradually increases. The cross-sensitivity generated by mode-localized and constant-drive methods are 28.7% and 1.1%, respectively.

Discussion

This paper introduces a constant-drive method that enables the simultaneous detection of two signals by a three-degree-of-freedom WCRs. Unlike existing three-degree-of-freedom mode-localized sensors³¹, where the stiffness of the middle resonator is set much higher than that of the other two to reduce coupling and enhance sensitivity, this study equalizes the stiffness of all three resonators and measures their vibration amplitudes. In previously reported designs, only the two outer resonators typically participate in signal detection, and therefore, they can only detect a single signal.

This study is the first to provide a theoretical analysis of the signal interference mechanism in WCRs, explaining the underlying causes. When multiple signals are input, each one induces a shift in the resonance frequency of the WCRs, which in turn causes changes in the vibration amplitude of each resonator. This results in significant cross-sensitivity between the different signals.

This study employs the first-order natural frequency of weakly coupled resonators (WCRs) for constant-drive operation to reduce cross-sensitivity. The analysis is conducted through theoretical modeling, FEM simulation, and experimental validation. The theoretical analysis shows that, without considering damping, the constant-drive method can completely eliminate signal interference, reducing cross-sensitivity to zero, while the mode-localized method yields a cross-sensitivity of 25.8%. FEM simulations, accounting for damping, reveal that the constant-drive method achieves a cross-sensitivity of just 0.054%. Experimental validation further confirmed the method's effectiveness, with cross-sensitivity between the two signals measured at 3.1% and 1.1%, respectively. Additionally, results from the

theoretical analysis, FEM simulation, and experiments all demonstrate that the sensitivity of the constant-drive method is nearly identical to that of the mode-localized method, preserving the high sensitivity characteristics of mode-localized sensors.

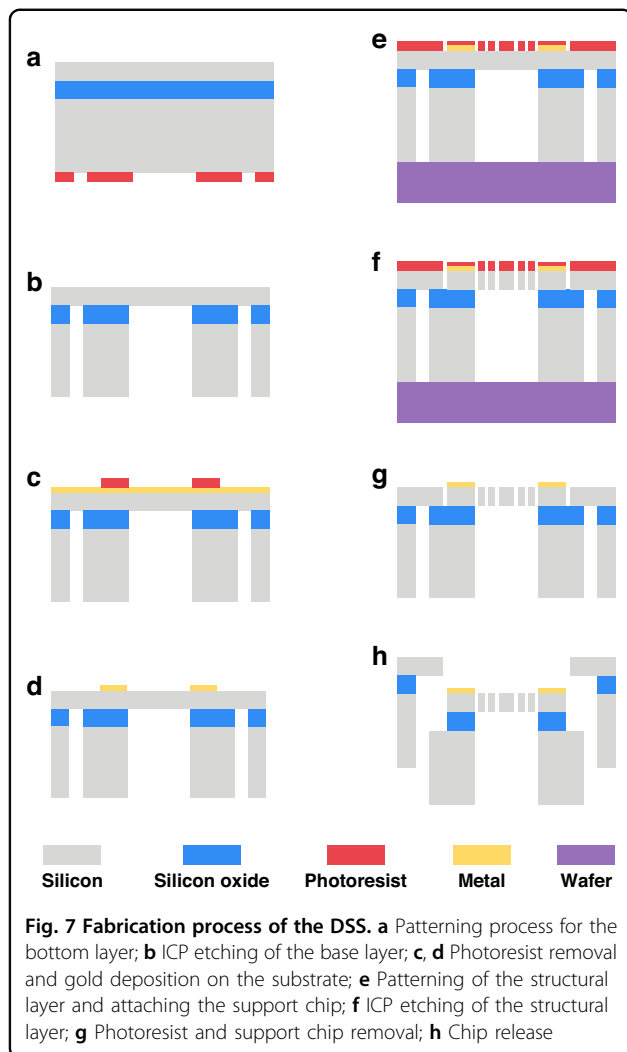
The experimentally measured reduction in cross-sensitivity did not fully align with the theoretical and simulation results, likely due to factors such as manufacturing tolerances, residual stress, and environmental influences. Fabrication imperfections may introduce asymmetries in resonator geometry and coupling stiffness, which can increase the feedthrough current and amplify cross-sensitivity. Additionally, residual stress may disrupt the coupling balance, resulting in a significant difference in detection sensitivity between the two signals. Furthermore, external disturbances, including temperature fluctuations and mechanical vibrations, can affect the vibration state of resonator, introducing additional cross-sensitivity not accounted for in simulations. Despite the differences between theory and experiment, the experimentally measured cross-sensitivity of the DSS reached levels comparable to similar devices, such as biaxial accelerometers^{32–35}, demonstrating its practical application value.

The method proposed in this paper is a general approach that utilizes constant-frequency drive and can be applied to almost any coupled resonator-based sensor. By modifying the front-end sensing structure and changing the voltage input to force or electric field input, the system can be adapted into a multi-axis force or electric field sensor. Additionally, by designing the resonators in a vertical configuration, the method can be extended to a biaxial accelerometer. Compared to standalone mode-localized sensors, this approach is expected to have lower power consumption due to the elimination of complex frequency-tracking circuitry.

This study validates the potential of the constant-drive method to advance the development of sensors based on weakly coupled resonators, marking a significant contribution to the field.

Conclusion

This study presents a novel approach for the synchronous detection of dual signals using a three-degree-of-freedom weakly coupled resonator system. By utilizing a mode-locking technique, we effectively decouple the interactions between multiple signals, thereby eliminating crosstalk and enhancing sensitivity. The experimental and finite element analysis results demonstrate that the constant-drive mode maintains sensitivity comparable to closed-loop modal localization methods while ensuring minimal interference between the signals. This advancement not only broadens the functional capabilities of MEMS sensors but also offers a reliable solution for



applications requiring simultaneous detection of multiple parameters. The findings contribute significantly to the development of high-performance sensing technologies in various fields.

Materials and fabrication

The DSS was fabricated using a dicing-free silicon-on-insulator (SOI) process^{36,37} with a 50 μm thick device layer, as shown in Fig. 7. The process started with the formation of the back cavity, which reduced release time and minimized footing effects. AZ4620 was selected as the positive photoresist for the 450 μm base layer, with a thickness of 7–8 μm . The silicon wafer was etched in an ICP chamber down to the middle oxide layer, followed by immersion in acetone for 30 min to dissolve the photoresist.

Next, a metal layer was patterned, and gold (Au) electrodes were deposited at a thickness of 300 nm. The lateral corrosion error during Au removal was kept under 5 μm .

Photoresist was also used for the 3 μm structural layer, and the silicon wafer was bonded to the support, applying uniform pressure to ensure proper adhesion and avoid gaps that could affect thermal conductivity.

Afterward, the silicon wafer was etched to the middle oxide layer, as shown in Fig. 7h, separating the DSS chip from the wafer frame. The bonded wafers were then immersed in acetone for 30 min to release the silicon from the supporting wafers. Finally, the box layer self-separated, allowing the device and support to detach after the box layer release.

Acknowledgements

This work was supported by the National Science Foundation of China (No. 52435012 and No. 52475606), the National Key Research and Development Program of China (No. 2023YFB3208800), Innovation Capability Support Program of Shaanxi (No. 2024RS-CXTD-7), and the Fundamental Research Funds for the Central Universities.

Author contributions

H.L. fabricated the devices and tested the device. Z.Z. helped complete the experimental test and designed the interface circuit. P.Y.Z. and G.H.Z. helped with data processing. Dr. Y.C.H. revised the manuscript, and Prof. H.L.C. proposed the idea and guided the entire work.

Conflict of interest

The authors declare no competing interests.

Received: 2 January 2025 Revised: 19 March 2025 Accepted: 13 April 2025
Published online: 09 May 2025

References

- Bogue, R. Recent developments in MEMS sensors: a review of applications, markets and technologies. *Sens. Rev.* **33**, 300–304 (2013).
- Shin, S. H. et al. Integrated arrays of air-dielectric graphene transistors as transparent active-matrix pressure sensors for wide pressure ranges. *Nat. Commun.* **8**, 14950 (2017).
- Wang, Z. L. Self-powered nanosensors and nanosystems. *Adv. Mater.* **24**, 280–285 (2012).
- Guo, Y., Zhong, M. J., Fang, Z. W., Wan, P. B. & Yu, G. H. A wearable transient pressure sensor made with MXene nanosheets for sensitive broad-range human-machine interfacing. *Nano Lett.* **19**, 1143–1150 (2019).
- Chorsi, M. T. et al. Piezoelectric biomaterials for sensors and actuators. *Adv. Mater.* **31**, e1802084 (2019).
- Luo, R. C., Chang, C. C. & Lai, C. C. Multisensor fusion and integration: Theories, applications, and its perspectives. *IEEE Sens. J.* **11**, 3122–3138 (2011).
- Wu, J. E. et al. Review of high temperature piezoelectric materials, devices, and applications. *Acta Phys. Sin.* **67**, 207701 (2018).
- Spletzer, M., Raman, A., Wu, A. Q., Xu, X. & Reifenberger, R. Ultrasensitive mass sensing using mode localization in coupled microcantilevers. *Appl. Phys. Lett.* **88**, 254102 (2006).
- Giesen, F., Podbielski, J. & Grundler, D. Mode localization transition in ferromagnetic microscopic rings. *Phys. Rev. B* **76**, 014431 (2007).
- Hodges, C. H. Confinement of vibration by structural irregularity. *J. Sound Vib.* **82**, 411–424 (1982).
- Hodges, C. H. & Woodhouse, J. Theories of noise and vibration transmission in complex structures. *Rep. Prog. Phys.* **49**, 107–170 (1986).
- Hodges, C. H. & Woodhouse, J. Confinement of vibration by one-dimensional disorder. 1. theory of ensemble averaging. *J. Sound Vib.* **130**, 237–251 (1989).
- Anderson, P. W. Absence of diffusion in certain random lattices. *Phys. Rev.* **109**, 1492–1505 (1958).
- Zhang, H. et al. Mode-localized accelerometer in the nonlinear duffing regime with 75 ng bias instability and 95 ng/ $\sqrt{\text{Hz}}$ noise floor. *Microsyst. Nanoeng.* **8**, 17 (2022).

15. Kang, H., Ruan, B., Hao, Y. C. & Chang, H. L. Mode-localized accelerometer with ultrahigh sensitivity. *Sci. China Inf. Sci.* **65**, 142402 (2022).
16. Zhang, H. et al. A low-noise high-order mode-localized MEMS accelerometer. *J. Microelectromechanical Syst.* **30**, 178–180 (2021).
17. Zhang, H. et al. A mode-localized MEMS accelerometer in the modal overlap regime employing parametric pump. In *21st International Conference on Solid-State Sensors, Actuators and Microsystems (Transducers)*. 108–111 (2021).
18. Zhang, H. et al. A high-performance mode-localized accelerometer employing a quasi-rigid coupler. *IEEE Electron Device Lett.* **41**, 1560–1563 (2020).
19. Pandit, M. et al. A mode-localized MEMS accelerometer with 7 μ g bias stability. In *31st IEEE International Conference on Micro Electro Mechanical Systems (MEMS)*. 968–971 (IEEE, 2018).
20. Li, X. D. et al. Mode-localized cantilever array for picogram order mass sensing. In *12th IEEE Annual International Conference on Nano/Micro Engineered and Molecular Systems (IEEE-NEMS)*. 587–590 (IEEE, 2017).
21. Kang, H., Ruan, B., Hao, Y. C. & Chang, H. L. A micromachined electrometer with room temperature resolution of 0.256 e $\sqrt{\text{Hz}}$. *IEEE Sens. J.* **20**, 95–101 (2020).
22. Zhang, H. et al. A high-sensitive resonant electrometer based on mode localization of the weakly coupled resonators. In *29th IEEE International Conference on Micro Electro Mechanical Systems (MEMS)*. 87–90 (IEEE, 2016).
23. Zhao, J. X., Ding, H. & Xie, J. Electrostatic charge sensor based on a micro-machined resonator with dual micro-levers. *Appl. Phys. Lett.* **106**, 233505 (2015).
24. Thiruvengatanathan, P., Yan, J. & Seshia, A. A. Ultrasensitive mode-localized micromechanical electrometer. In *2010 IEEE International Frequency Control Symposium*. 91–96 (IEEE, 2010).
25. Hao, Y. C. et al. A mode-localized DC electric field sensor. *Sens. Actuators A Phys.* **333**, 113244 (2022).
26. Li, H., Zhang, Z., Zu, L., Hao, Y. & Chang, H. Micromechanical mode-localized electric current sensor. *Microsyst. Nanoeng.* **8**, 42 (2022).
27. Hao, Y. C., Liang, J. J., Kang, H., Yuan, W. Z. & Chang, H. L. A micromechanical mode-localized voltmeter. *IEEE Sens. J.* **21**, 4325–4332 (2021).
28. Guo, X., Yang, B., Li, C. & Liang, Z. Y. Enhancing output linearity of weakly coupled resonators by simple algebraic operations. *Sens. Actuators A Phys.* **325**, 112696 (2021).
29. Zhang, H., Chang, H. & Yuan, W. Characterization of forced localization of disordered weakly coupled micromechanical resonators. *Microsyst. Nanoeng.* **3**, 1–9 (2017).
30. Kang, H., Yang, J. & Chang, H. A closed-loop accelerometer based on three degree-of-freedom weakly coupled resonator with self-elimination of feed-through signal. *IEEE Sens. J.* **18**, 3960–3967 (2018).
31. Zhao, C. et al. A three degree-of-freedom weakly coupled resonator sensor with enhanced stiffness sensitivity. *J. Microelectromechanical Syst.* **25**, 38–51 (2016).
32. Caspani, A., Comi, C., Corigliano, A., Langfelder, G. & Tocchio, A. Compact biaxial micromachined resonant accelerometer. *J. Micromech. Microeng.* **23**, 105012 (2013).
33. Yang, B., Zhao, H., Dai, B. & Liu, X. A new silicon biaxial decoupled resonant micro-accelerometer. *Microsyst. Technol. Micro Nanosyst. Inf. Storage Process. Syst.* **21**, 109–115 (2015).
34. Ding, H., Zhao, J., Ju, B.-F. & Xie, J. A high-sensitivity biaxial resonant accelerometer with two-stage microleverage mechanisms. *J. Micromech. Microeng.* **26**, 015011 (2016).
35. Shin, S. et al. A dual-axis resonant accelerometer based on electrostatic stiffness modulation in epi-seal process. In *18th IEEE Sensors Conference* (IEEE, 2019).
36. Hao, Y., Xie, J., Yuan, W. & Chang, H. Dicing-free SOI process based on wet release technology. *Micro Nano Lett.* **11**, 775–778 (2016).
37. Hao, Y., Wang, Y., Liu, Y., Yuan, W. & Chang, H. An SOI-based post-fabrication process for compliant MEMS devices. *J. Micromech. Microeng.* **34**, 045005 (2024).